

# Trace doping of multiple elements enables stable battery cycling of LiCoO<sub>2</sub> at 4.6 V

Jie-Nan Zhang<sup>1,2,9</sup>, Qinghao Li<sup>1,3,9</sup>, Chuying Ouyang<sup>4</sup>, Xiqian Yu<sup>1,2\*</sup>, Mingyuan Ge<sup>5</sup>, Xiaojing Huang<sup>5</sup>, Enyuan Hu<sup>5</sup>, Chao Ma<sup>6</sup>, Shaofeng Li<sup>7</sup>, Ruijuan Xiao<sup>1</sup>, Wanli Yang<sup>3</sup>, Yong Chu<sup>5</sup>, Yijin Liu<sup>7\*</sup>, Huigen Yu<sup>8</sup>, Xiao-Qing Yang<sup>5</sup>, Xuejie Huang<sup>1</sup>, Liquan Chen<sup>1</sup> and Hong Li<sup>1,2\*</sup>

**LiCoO<sub>2</sub> is a dominant cathode material for lithium-ion (Li-ion) batteries due to its high volumetric energy density, which could potentially be further improved by charging to high voltages. However, practical adoption of high-voltage charging is hindered by LiCoO<sub>2</sub>'s structural instability at the deeply delithiated state and the associated safety concerns. Here, we achieve stable cycling of LiCoO<sub>2</sub> at 4.6 V (versus Li/Li<sup>+</sup>) through trace Ti-Mg-Al co-doping. Using state-of-the-art synchrotron X-ray imaging and spectroscopic techniques, we report the incorporation of Mg and Al into the LiCoO<sub>2</sub> lattice, which inhibits the undesired phase transition at voltages above 4.5 V. We also show that, even in trace amounts, Ti segregates significantly at grain boundaries and on the surface, modifying the microstructure of the particles while stabilizing the surface oxygen at high voltages. These dopants contribute through different mechanisms and synergistically promote the cycle stability of LiCoO<sub>2</sub> at 4.6 V.**

The constantly increasing energy consumption of modern society has led to the demand for energy storage technology with higher energy densities<sup>1–3</sup>. Li-ion batteries (LIBs) are the most popular energy storage devices, which are widely deployed in portable electronics and, more recently, in electric vehicles. The energy density of LIBs is directly proportional to the working voltage and lithium storage capacity. Therefore, the development of cathode materials that are of larger reversible capacity and compatible with higher voltage charging has been a hot research topic<sup>4–7</sup>. Thanks to the tremendous research efforts devoted over the past few decades, we have witnessed the successful commercialization of quite a number of cathode materials (see the comparison of their theoretical energy densities in Supplementary Fig. 1). We note here that LiCoO<sub>2</sub>, which was first recognized as a cathode material with good potential in the 1980s, still presents competitive or even superior energy density among all of the cathode materials that are commercially available. As a key player on today's market of cathode materials, LiCoO<sub>2</sub> exhibits many essential advantages, including high theoretical capacity, Li<sup>+</sup>/electron conductivity, theoretical density and compressed electrode density<sup>8–10</sup>. While the theoretical capacity of LiCoO<sub>2</sub> is as high as 274 mAh g<sup>-1</sup>, its practical discharge capacity with an acceptable level of cycle reversibility is only about 173 mAh g<sup>-1</sup> (Li<sub>1-x</sub>CoO<sub>2</sub>, x = ~0.63; 4.45 V versus Li/Li<sup>+</sup>). Increasing the charging cut-off voltage to extract more Li<sup>+</sup> can further increase the capacity of LiCoO<sub>2</sub> (for example, 4.5 V versus Li/Li<sup>+</sup> gives a 6.9% increase in capacity (~185 mAh g<sup>-1</sup>) and 4.6 V versus Li/Li<sup>+</sup> gives a 27.2% increase in capacity (~220 mAh g<sup>-1</sup>); however, such practice could lead to several detrimental problems, causing rapid decay of cycle efficiency and capacity. More specifically, when the voltage reaches 4.5 V, a harmful phase transformation from the O3 hexagonal phase to the hybridized O1–O3 hexagonal phase (denoted as the

H1–3 phase, where O represents octahedral sites, 3 is the stacking sequence of oxygen layers ABCABC, and 1 represents ABAB) occurs and is accompanied by gliding of the lattice slabs and partial collapse of the O3 lattice structure<sup>11</sup>. Consequently, the internal strain builds up, leading to crack formation and particle pulverization<sup>11,12</sup>. Meanwhile, oxygen loss at high voltage further brings irreversible phase transition or even safety concerns. Besides these structural failure modes in the bulk, the surface instability is another critical issue that is amplified at the high state of charge. The high-valence Co/O could trigger undesired interfacial side reactions, involving oxidization of the electrolyte. All of these factors add up to serious performance degradation of LiCoO<sub>2</sub> at high voltage, jeopardizing the practical application of the significantly increased capacity<sup>13–16</sup>.

Many strategies have been considered to promote the cycle stability of LiCoO<sub>2</sub> at high voltage<sup>17–21</sup>. Among various approaches, foreign element doping is the most prevailing and has been demonstrated to be promising and effective for the improvement of electrochemical performances of LiCoO<sub>2</sub><sup>22–25</sup>. For example, a study compared the cycle performances of doped LiCoO<sub>2</sub> at a high charging voltage of 4.5 V with various transition metal ions (LiTM<sub>0.05</sub>Co<sub>0.95</sub>O<sub>2</sub>, where TM = Mn, Fe, Cu or Zn)<sup>26</sup>, and found that Mn doping enhanced the reversible capacity the most, to ~158 mAh g<sup>-1</sup>, compared with ~138 mAh g<sup>-1</sup> for bare LiCoO<sub>2</sub> after 50 cycles in the voltage range of 3.5–4.5 V. It has also been reported that concurrent doping of La and Al can greatly improve the Li diffusivity and structure stability of LiCoO<sub>2</sub><sup>16</sup>. With such a doping strategy, LiCoO<sub>2</sub> can achieve a high capacity of 190 mAh g<sup>-1</sup> over 50 cycles at a high cut-off voltage of 4.5 V. Here, we point out that, while these previous works instinctively assume that the dopants are well incorporated into the parent lattice, theoretical calculations have predicted limited solubility of foreign atoms in LiCoO<sub>2</sub> in some cases<sup>27</sup>. Such inconsistencies

<sup>1</sup>Beijing Advanced Innovation Center for Materials Genome Engineering, Institute of Physics, Chinese Academy of Sciences, Beijing, China. <sup>2</sup>Center of Materials Science and Optoelectronics Engineering, University of Chinese Academy of Sciences, Beijing, China. <sup>3</sup>Advanced Light Source, Lawrence Berkeley National Laboratory, Berkeley, CA, USA. <sup>4</sup>Laboratory of Computational Materials Physics, Department of Physics, Jiangxi Normal University, Jiangxi, China. <sup>5</sup>Brookhaven National Laboratory, Upton, NY, USA. <sup>6</sup>College of Materials Science and Engineering, Hunan University, Changsha, China. <sup>7</sup>Stanford Synchrotron Radiation Lightsource, SLAC National Accelerator Laboratory, Menlo Park, CA, USA. <sup>8</sup>Beijing WeLion New Energy Technology, Beijing, China. <sup>9</sup>These authors contributed equally: Jie-Nan Zhang, Qinghao Li. \*e-mail: [xyu@iphy.ac.cn](mailto:xyu@iphy.ac.cn); [liyujin@slac.stanford.edu](mailto:liyujin@slac.stanford.edu); [hli@iphy.ac.cn](mailto:hli@iphy.ac.cn)

necessitate in-depth investigations of the fundamental roles of various dopants in improving battery performances. Compared with the literature reports based on laboratory-scale experiments, it is worth noting that the doping concentration is generally two to three orders of magnitude lower for industrial production. Therefore, for LiCoO<sub>2</sub> with low-concentration doping at a level of industrial relevance, empirical accumulation is of vital significance and the corresponding fundamental research is urgently needed. Moreover, co-doping with multiple elements is commonly executed in practice. The desired synergistic effect among multiple dopants needs further exploration, but the characterizations of multiple doping elements at low concentrations are daunting and challenging.

In this work, we show that trace amounts of Ti–Mg–Al co-doping (~0.1 wt% for each dopant) can greatly improve the cycle and rate performances of LiCoO<sub>2</sub> at a high charging cut-off voltage of 4.6 V. The fundamental roles of each individual dopant in promoting the electrochemical performances are systematically studied by combining various characterization techniques, including synchrotron X-ray spectroscopy and X-ray imaging. We find that Al and Mg atoms are successfully incorporated into the LiCoO<sub>2</sub> lattice and can effectively suppress the detrimental phase transition at high charging voltages (above 4.5 V). However, even at trace amounts, Ti segregates at the grain boundaries and on the particle surface, facilitating fast lithium diffusion and alleviating internal strain within the assembled LiCoO<sub>2</sub> particle. Moreover, the Ti-rich surface can stabilize the oxygen redox and inhibit the undesired electrode–electrolyte interfacial reactions. These experimental findings are further explained by first-principles calculations, showing that the extraordinary battery performance of Ti–Mg–Al co-doped LiCoO<sub>2</sub> can be attributed to both microstructure changes and electronic structure reconfiguration induced by co-doping with trace amounts of Ti, Mg and Al.

### Characterizations of bare LCO and TMA-LCO

Undoped LiCoO<sub>2</sub> (bare LCO), Ti, Mg or Al single-element-doped LiCoO<sub>2</sub>, and Ti–Mg–Al co-doped LiCoO<sub>2</sub> (TMA-LCO) were prepared using a solid-state reaction method. The inductively coupled plasma emission spectroscopy results in Supplementary Table 1 indicate that the actual chemical compositions of these as-synthesized materials agree well with the intended compositions. Diverse characterizations of the synthesized materials were performed, and the results are summarized in Supplementary Tables 2–4 and Supplementary Figs. 2–4. It is evident that foreign-atom doping has a significant influence on various aspects of the physical properties of LiCoO<sub>2</sub>, such as structural parameters, particle size, morphology and conductivity. The doping elements—especially Ti—can introduce lattice strain and slightly reduce the particle size of LiCoO<sub>2</sub>. Moreover, Mg doping causes an increase in electronic conductivity, whereas Al doping has minimal impact on these physical parameters.

Here, we focus on TMA-LCO, which shows the best electrochemical performances. The Rietveld refinements of X-ray diffraction patterns of bare LCO and TMA-LCO indicate a pure *R-3m* layered structure with negligible differences in lattice parameters (Supplementary Fig. 2 and Supplementary Table 4). As shown in Fig. 1a,b, the primary particle size of TMA-LCO (that is, the diameter at which 50% of a sample's mass comprises smaller particles (D50): ~15 μm) is slightly smaller than that of bare LCO (D50: ~16 μm). Further elemental mappings of the local region over a TMA-LCO particle show an overall homogeneous distribution of the foreign elements Ti, Mg and Al (Fig. 1d), except for the Ti-rich edge region. In view of the resolution limit of elemental mapping, energy-dispersive X-ray spectroscopy (EDS) and electron energy loss spectroscopy (EELS) measurements were carried out, revealing the slight differences in elemental concentration between the centre and edge areas of the TMA-LCO particle. As highlighted in Fig. 1e,f, both EDS and EELS results show that Ti has a higher

elemental concentration at the surface than in the interior of the particle, but there is no evident difference for Mg and Al. To further confirm this phenomenon, elemental distribution near the particle edge in a finer area was analysed. The high-angle annular dark-field image and elemental mappings near the particle edge of the cross-sectional transmission electron microscopy (TEM) sample are shown in Supplementary Fig. 5, which shows Ti aggregation at the particle surface. X-ray photoelectron spectroscopy (XPS) etching results further confirm the heterogeneity of the spatial distribution of Ti within the particles (Supplementary Fig. 6).

### Electrochemical performances

The electrochemical performances of bare LCO and TMA-LCO were evaluated in both half cells and full cells, and the results are displayed in Fig. 2a–e and Supplementary Figs. 7 and 8 (initial charge–discharge curves and cycle versus rate performances, respectively). It is apparent that TMA-LCO presents improved cycle stability in half cells compared with bare LCO, in particular at the high-charging cut-off voltage of 4.6 V. A high reversible discharge capacity of 174 mAh g<sup>-1</sup>, with capacity retention of 86% (compared with the second cycle), is achieved in TMA-LCO after 100 cycles at a current rate of 0.5 C (1 C = 274 mA g<sup>-1</sup>; note that all cells were cycled at 0.1 C for the formation process at the first cycle). The Coulombic efficiency was also recorded during electrochemical cycling. The TMA-LCO cell shows slightly higher Coulombic efficiency (93.7%) than the bare LCO cell (90.2%) at 4.6 V charging for the first cycle, quickly increases to 99% after three cycles and remains stable for the subsequent cycles (Supplementary Fig. 9). The charge–discharge profiles at selected cycle numbers are presented in Fig. 2b,c. It can be seen that bare LCO has significantly degraded voltage profiles after 50 cycles, indicating the more severe structural degradation in bare LCO than TMA-LCO. The cycle and rate performances of single-element-doped LiCoO<sub>2</sub> were also evaluated, and the results are shown in Supplementary Fig. 8. They all show better cycle and rate performances than bare LCO, but inferior performances to TMA-LCO.

For potential practical applications, full pouch cells (~2.8 Ah) with bare LCO or TMA-LCO cathodes and commercial graphite anodes were assembled and cycled at room temperature in the voltage range of 3.0–4.55 V (equivalent to 4.6 V versus Li/Li<sup>+</sup>). As shown in Fig. 2d, the capacity of bare LCO fades quickly to 51.3 mAh g<sup>-1</sup> after 70 cycles. In contrast, the TMA-LCO cell shows much improved capacity retention with a capacity of 178.2 mAh g<sup>-1</sup> after 70 cycles, and a much more stable Coulombic efficiency than that of bare LCO (Supplementary Fig. 10). The discharge voltage remains almost unchanged at around 3.90 V for TMA-LCO, while it gradually drops to 3.51 V for bare LCO. The seriously degraded cycle performance of the bare LCO full cell can be attributed to the irreversible structural transformation and unwanted side reactions, which can be further proved by the obvious gas generation in the cycled pouch cell, as shown in the inset of Fig. 2e. Overall, TMA-LCO shows greatly improved electrochemical performances in both the half cell and the full cell at a high charging cut-off voltage of 4.6 V (versus Li/Li<sup>+</sup>) compared with bare LCO (a comparison of the performances with reports in the literature for high-voltage LiCoO<sub>2</sub> is provided in Supplementary Tables 5 and 6).

### Structural evolution during first charge–discharge process

As the cycle stability of LiCoO<sub>2</sub> is strongly associated with its structural evolution, in situ X-ray diffraction (XRD) experiments were performed to study the phase transition behaviour. Although pristine bare LCO and TMA-LCO share a similar crystal structure, distinct differences in structural evolution over the first charge–discharge process can be observed, as shown in Fig. 3a,b. The (003) and (107) diffraction peaks were selected for demonstration. A relatively small (003) peak shift is observed in TMA-LCO at a high voltage of

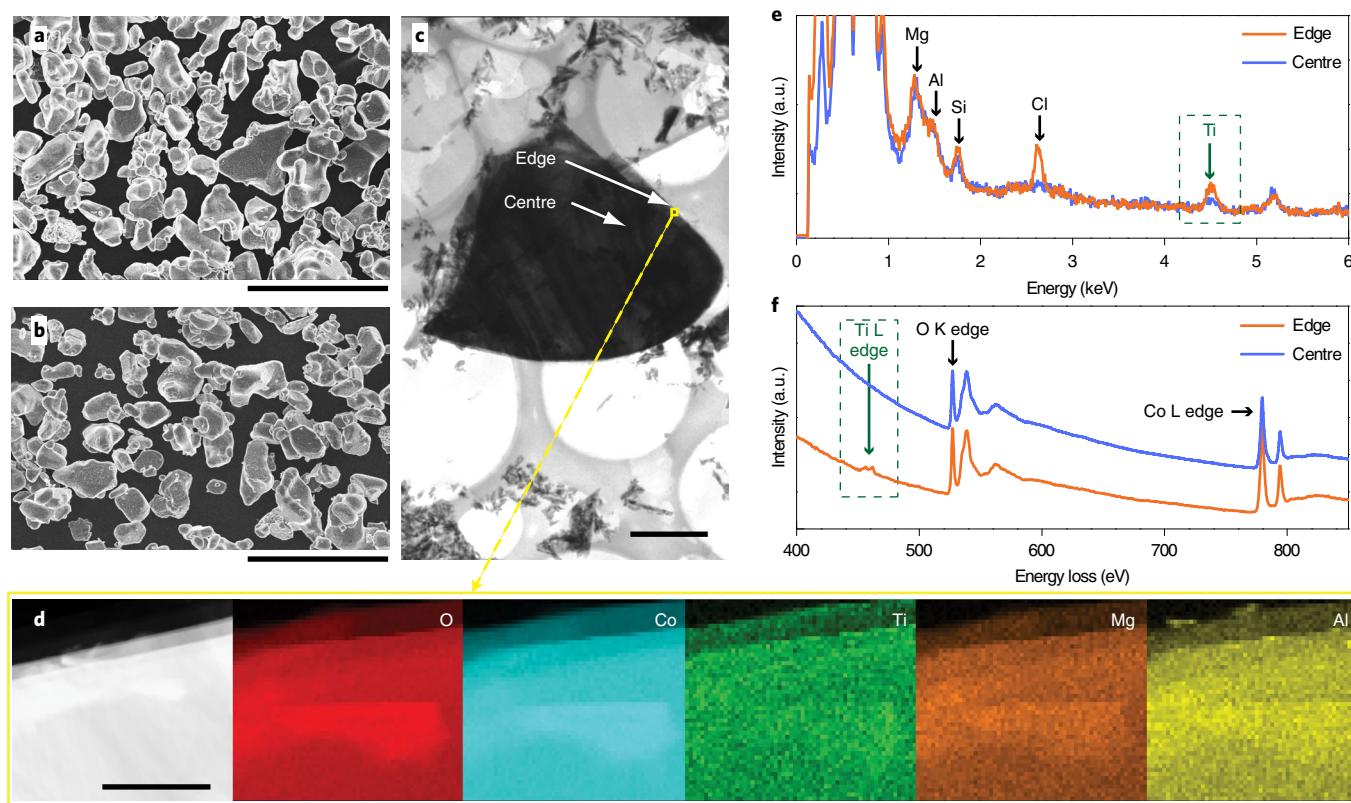


**Fig. 1 | Morphology and elemental distribution in bare LCO and TMA-LCO.** **a, b**, Scanning electron microscopy (SEM) images of bare LCO (**a**) and TMA-LCO (**b**). Scale bars: 20  $\mu\text{m}$ . **c**, Cross-sectional TEM image of TMA-LCO. Scale bar: 2  $\mu\text{m}$ . **d**, High-angle annular dark-field scanning TEM image and EDS elemental mappings of O, Co, Ti, Mg and Al (scale bar: 100 nm) in the selected region indicated by the yellow rectangle in **c**, showing an overall homogeneous distribution of the doping elements Ti, Mg and Al, except for the Ti-rich edge region (see the enlarged images and integrated intensity profiles in Supplementary Fig. 5). **e, f**, EDS (**e**) and EELS spectra (**f**), collected separately from the edge (surface) and centre (interior) regions of TMA-LCO, as indicated by the white arrows in **c**. The green dashed rectangle highlights the signal of Ti, revealing the slightly increased concentration of Ti in the edge region compared with the centre region in the TMA-LCO particle.

4.6 V, in contrast with the dramatic (003) peak shift in bare LCO. This could be attributed to the suppressed O3 to H1-3 phase transition, which is accompanied by the oxygen stacking sequence change (Fig. 3d)<sup>28,29</sup>. Such mitigation of structural changes is also shown in the (107) peak shift, as highlighted by the vertical dotted lines in Fig. 3a, b. The (107) peak splitting at 4.1 V occurs in both bare LCO and TMA-LCO, and can be attributed to an order-disorder transition<sup>30,31</sup>. Considering the superior battery performance of TMA-LCO, the conversion between the hexagonal and monoclinic phases at around 4.1 V may not be the main cause of performance degradation. The phase transition behaviour also manifests itself in the charge-discharge voltage profiles and cyclic voltammetry curves of bare LCO and TMA-LCO, which are shown in Fig. 3c. The persistence of the anodic and cathodic peaks due to the order-disorder transition and the difference between bare LCO and TMA-LCO at a high voltage of 4.6 V are consistent with the in situ XRD results.

### 3D elemental distributions in the TMA-LCO particle

Considering the indication of a non-uniform dopant distribution from the EDS and EELS results, it is necessary to determine the actual spatial distribution of the key elements in the  $\text{LiCoO}_2$  particles. X-ray fluorescence mapping, which is capable of detecting the spatial elemental distribution and concentration with high sensitivity, was utilized to probe the 3D elemental distribution within an arbitrarily selected TMA-LCO particle. Because Mg was outside of the working energy window, only Al, Co and Ti signals were collected, and the 3D renderings of their distributions are displayed

in Fig. 4a–c. Figure 4d–f shows the elemental distributions over a virtual  $x$ - $z$  slice through the centre of the particle. The absolute concentrations of these elements are very different, as indicated by the coloured scale bar in the corresponding insets. It is evident from Fig. 4a, d that Al is homogeneously distributed throughout the entire particle, with a minor degree of concentration variation. In contrast, the Ti distribution presented in Fig. 4c, f shows a large degree of segregation. The Ti-rich phase forms a complex interconnected network (as highlighted by the dashed lines in Fig. 4f), dividing the  $\text{LiCoO}_2$  particle into several subdomains. For further evaluation of the subdomain separation effect, we first calculated the Ti-to-Co ratio, voxel by voxel, throughout the entire 3D volume. Areas with a Ti-to-Co ratio equal to or below the nominal value are segmented as active subdomains. As shown in Fig. 4g, 50 subdomains were identified and visualized. Note that different colours are used to distinguish adjacent subdomains for visualization. However, colours are reused for subdomains that are far apart, due to the large number of subdomains identified. Further quantification of these subdomains suggests that they have a wide distribution in volume and surface area, as indicated by Fig. 4h, i. Compared with the entire particle as a whole, the subdomains with largely reduced size and significantly increased surface area ensure fast  $\text{Li}^+$  diffusion in the micro-sized particles, which could be one major factor responsible for the improved rate performance of TMA-LCO. In addition, the subdomains separated by the Ti-rich phase can effectively reduce the lattice breathing induced by Li intercalation, and are more robust against lattice strain and particle fracture, thereby possibly

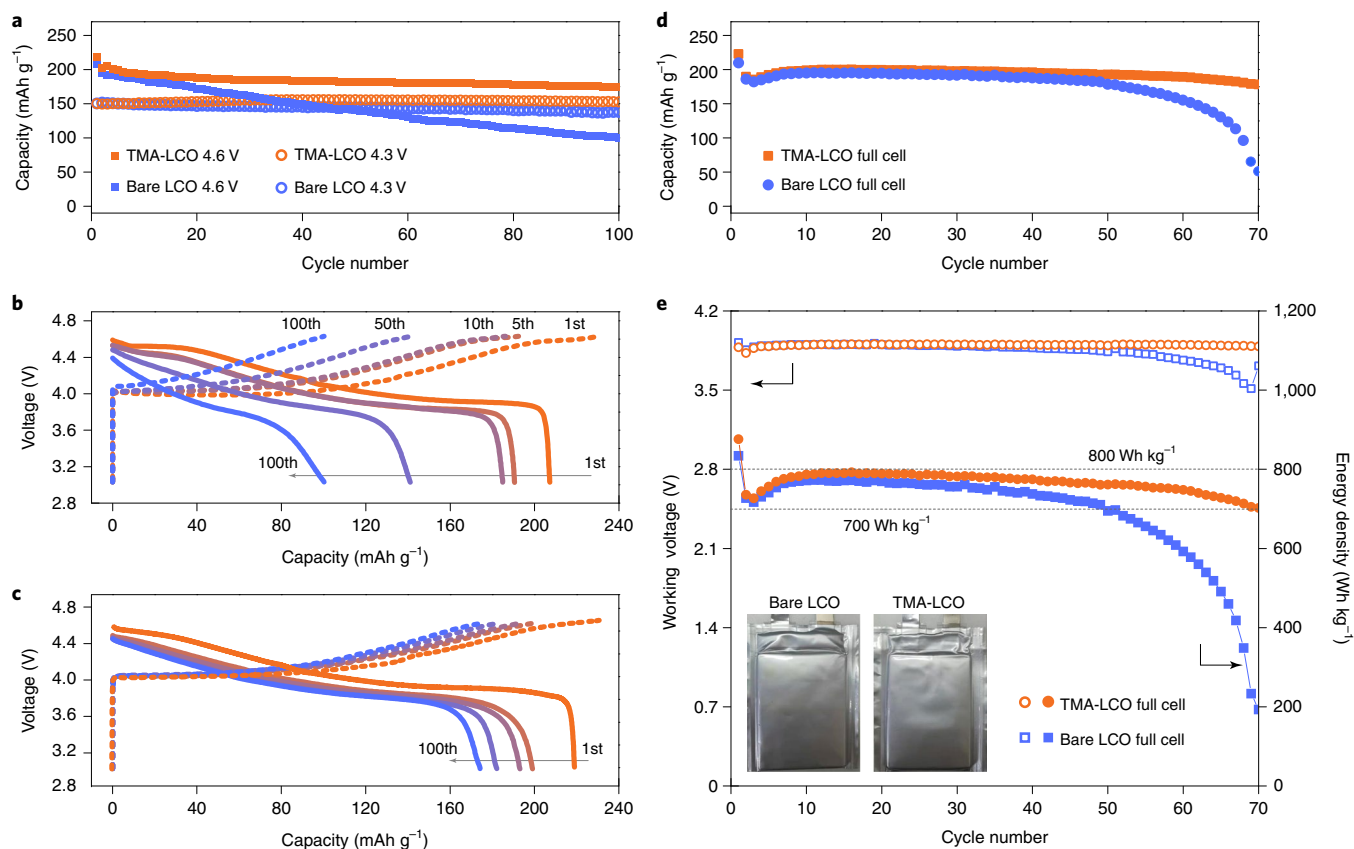


**Fig. 2 | Electrochemical characterization of bare LCO and TMA-LCO.** **a**, Comparison of cycle performances of LiCoO<sub>2</sub>|Li half cells with bare LCO versus TMA-LCO. **b,c**, Charge-discharge curves of bare LCO (**b**) and TMA-LCO (**c**) half cells for the 1st, 5th, 10th, 50th and 100th cycles. The charge and discharge tests were conducted at 0.1C for the first cycle and 0.5C for the subsequent cycles. **d**, Cycle performances of LiCoO<sub>2</sub>|graphite full cells with bare LCO versus TMA-LCO. A constant current and constant voltage mode was used for the full-cell tests. For the charge process, the cells were charged at 0.33C to 4.55V and then the voltage was held until the current dropped to 0.1C. The discharge current was 0.33C. **e**, Discharge voltage of the full cells and energy density of the cathode materials as a function of cycle number. Inset, pouch cells after the 70th cycle; obvious gas generation can be observed in the bare LCO|graphite pouch cell.

enhancing the long-term cycle stability of TMA-LCO. To ensure the representativeness of the conclusion drawn from the single particle analysis, we conducted 2D elemental mapping over many TMA-LCO particles using a synchrotron-based microprobe. The correlation evaluation and principle component analysis of the Co and Ti maps further confirm the heterogeneity distribution of Ti from a statistical point of view (Supplementary Fig. 11).

### Surface reaction probed by soft X-ray spectroscopy

Soft X-ray spectroscopy (sXAS) measurements were performed to study the surface properties of bare LCO and TMA-LCO<sup>32</sup>. Considering the strong correlation between oxygen involvement and battery failure at high voltage, the O K edge spectra are the research focus. Note that the strong hybridization between the transition metal 3*d* and O 2*p* states makes it challenging to separate the lattice oxygen signal from O K edge X-ray absorption spectroscopy (XAS)<sup>33</sup>. As a result, resonant inelastic X-ray scattering (RIXS; probing depth: ~150 nm), with extra resolution along the emission energy dimension, was selected as the tool of choice to clarify the role of oxygen<sup>34</sup>.

O K edge RIXS maps for bare LCO and TMA-LCO charged to 4.6V are shown in Fig. 5a,b, respectively, and the corresponding RIXS maps for pristine materials are shown in Supplementary Fig. 12. On deep delithiation, the most obvious change for bare LCO is the appearance of a well-distinguished isolated feature at an incident energy of 531 eV (Fig. 5a), indicating the oxidization

of O<sup>2-</sup> to a higher-valence state<sup>35</sup>. This RIXS feature becomes much weaker in TMA-LCO, indicating less participation of oxygen redox in the outer shell of TMA-LCO particles (in view of the probing depth of ~150 nm) compared with bare LCO, and the improved oxygen stability will also contribute to the enhanced safety behaviours at high voltage (Supplementary Figs. 13 and 14). Moreover, the RIXS spectra show the superior stability of TMA-LCO after 20 cycles compared with bare LCO, as shown in Fig. 5c. The elemental doping probably changes the intrinsic electronic structure, and consequently affects the redox reactions, particularly the oxygen redox chemistry.

The route of surface reactions with electrolyte may also be affected due to the different chemical reactivity of surface oxygen between bare LCO and TMA-LCO. Both XPS and sXAS results confirm the distinct cathode/electrolyte interphase (CEI) formed on bare LCO and TMA-LCO. As can be seen from the fitted O 1s XPS spectra in Fig. 5d, lattice oxygen (shaded area) shows a sharper peak that overwhelms signals from the CEI components in TMA-LCO compared with bare LCO, implying a relatively thinner and more stable CEI layer on TMA-LCO, as is schematically illustrated in Fig. 5e. Such an interpretation is also supported by quantitative analysis of XPS results, as shown in Supplementary Figs. 15 and 16 and Supplementary Table 7. Meanwhile, sXAS data collected in total electron yield (TEY) and total fluorescence yield (TFY) modes can provide further contrast between surface and bulk regions. Surface-sensitive TEY and bulk-sensitive TFY signals of TMA-LCO and

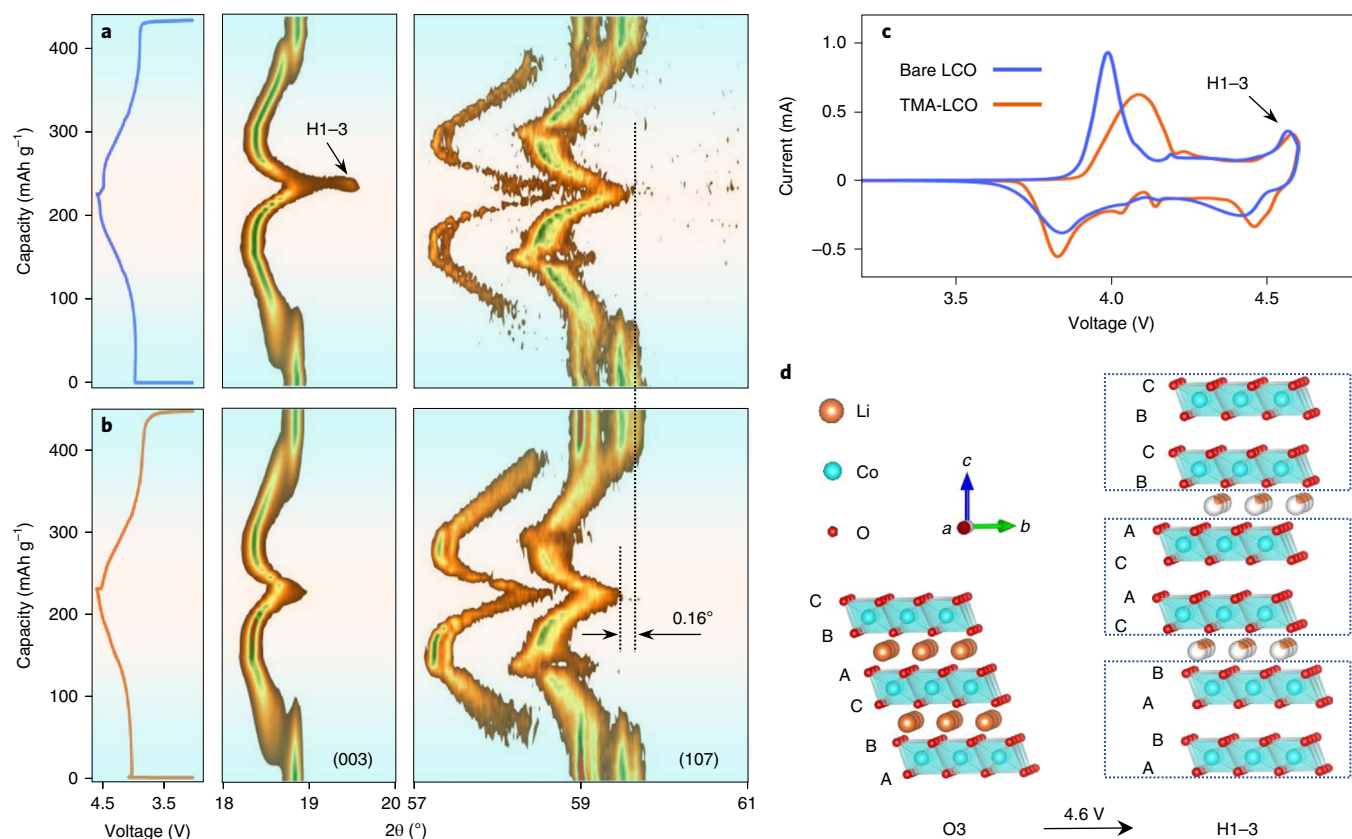


**Fig. 3 | Structural evolution during the initial charge-discharge process. a,b**, In situ XRD evolution of bare LCO (a) and TMA-LCO (b) at the (003) and (107) diffraction peaks, with the corresponding charge-discharge curves aligned to the left. A suppressed O3 to H1-3 phase transition with a smaller (107) diffraction peak shift ( $0.16^\circ$ ) can be observed for TMA-LCO at the 4.6 V charged state. **c**, Cyclic voltammetry results of bare LCO and TMA-LCO. **d**, Schematic of the atomic stacking of  $\text{Li}_x\text{CoO}_2$  in the O3 and H1-3 phases. For pristine  $\text{LiCoO}_2$ , the stacking can be described as being in the O3 phase, with an oxygen layer stacking sequence of ABCABC. On charging to 4.6 V, this sequence changes into ABABCACABCBC and the O3 to H1-3 phase transition occurs.

bare LCO in different cycle states are displayed as solid and dotted lines, respectively, in Supplementary Fig. 17. Note that the TEY spectra do not simply reproduce the TFY spectra, which can be attributed to interfacial reactions between the electrode and electrolyte. The relatively low pre-edge shoulder in TEY indicates the decrease of high valence Co at the particle surface, particularly for TMA-LCO. This phenomenon implies that different types of CEI layer form on TMA-LCO and bare LCO, which is consistent with the O 1s XPS results. The stable interface layer between cathode materials and electrolyte can also suppress the Co dissolution process (Supplementary Figs. 18–20). Therefore, the thinner and more stable CEI layer is expected to contribute to the superior electrochemical performances of TMA-LCO.

### Density functional theory and doping mechanisms

As Ti is rich on the surface of TMA-LCO, first principles calculations were conducted to gain a fundamental understanding of the Ti surface doping mechanism in  $\text{LiCoO}_2$ . To verify the experimental observations on Ti distribution, the optimized  $\text{LiCoO}_2$  (104) slab model was used (Fig. 6a). First, we considered replacing one Co atom from different layers of the slab with a Ti atom, and compared the total ground-state energies of Ti-doped  $\text{LiCoO}_2$  at different atomic layers, as listed in Supplementary Table 8. The Ti atom prefers to stay at the surface layer, rather than in the inner layers, with a 0.7 eV lower total energy. Then, we replaced two Co atoms at the surface layer with two Ti atoms, and considered the distribution of Ti atoms at the surface region. The different distances between the

nearest Ti atoms on the (104) surface are shown in Supplementary Fig. 21, and the total energies are listed in Supplementary Table 9. The results indicate the preference of Ti occupancy at the surface region. The incorporation of Ti into the  $\text{LiCoO}_2$  lattice alters the electronic structure as well. Figure 6b compares the  $2p$  states of the O atoms at the  $\text{LiCoO}_2$  (104) surface. Unoccupied O  $2p$  states can be observed for the surface O atoms for both Ti-doped and undoped  $\text{LiCoO}_2$  in the delithiated  $\text{Li}_{0.29}\text{CoO}_2$  state. However, the unoccupied states above the Fermi level are significantly suppressed after Ti doping, indicating suppressed charge deficiency in the surface layer. Figure 6c displays the relaxed structure of delithiated  $\text{Li}_{0.29}\text{CoO}_2$ , together with the charge density of the surface O atoms compared with lithiated  $\text{LiCoO}_2$ . The charge density contour clearly shows a substantial charge deficiency for the O atoms in the surface layer. The O atoms near the Ti atoms lose less charge compared with those far from the Ti atoms. Figure 6d shows the optimized atomic structure of Ti-doped  $\text{Li}_{0.29}\text{CoO}_2$ , where Ti atoms tend to stay in the surface layer. Charge analysis shows that the surface O atoms around Ti atoms hold more charge (are less oxidized), implying that Ti doping helps to resist the charge deficiency of the O atoms on delithiation. This agrees well with the aforementioned RIXS results.

### Conclusions

In summary, by virtue of Ti-Mg-Al co-doping, the physical properties of  $\text{LiCoO}_2$ , including the bulk crystal structure, electronic structure, particle shape and microstructure, are effectively

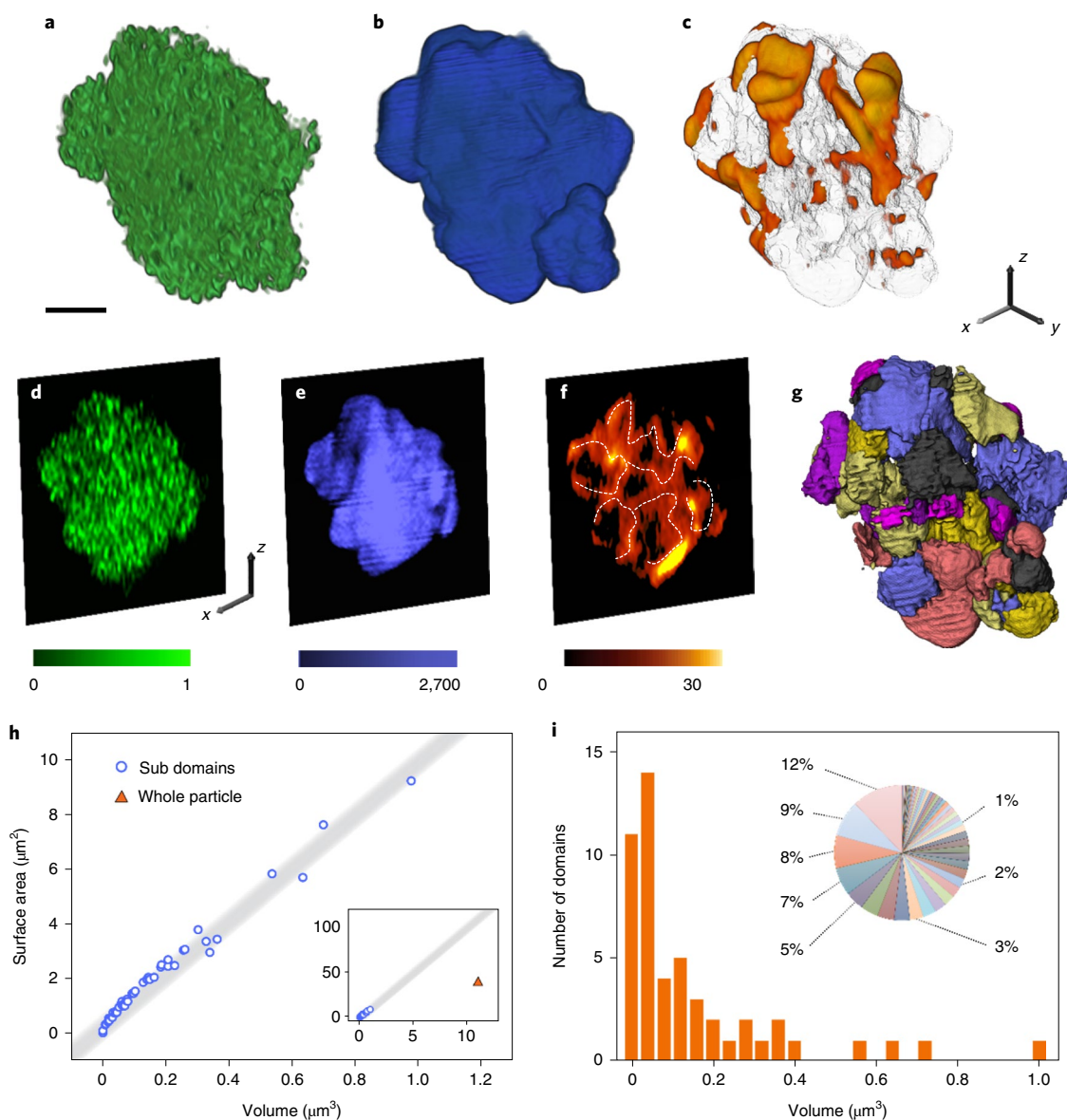


**Fig. 4 | 3D X-ray tomography reconstruction and element distribution in TMA-LCO.** **a–c**, 3D spatial distributions of Al (**a**), Co (**b**) and Ti (**c**), probed by fluorescence-yield scanning transmission X-ray microscopy. Scale bar: 1  $\mu\text{m}$ . **d–f**, Elemental distributions of Al (**d**), Co (**e**) and Ti (**f**) over the virtual  $x$ - $z$  slice through the centre of the particle. The green, blue and orange scale bars show counts. **g**, Identified and visualized subdomain formation. Note that different colours are used to distinguish between adjacent subdomains. **h**, Quantification of the volume and surface area of the subdomains and the entire particle as a whole (inset). The grey shadow is the linear trend extracted from the data for the subdomains. **i**, Volume distribution of all of the subdomains. Inset: volume fraction of each individual subdomain, highlighting the existence of a few large subdomains, which make up nearly 50% of the total volume, and a large number of small domains.

modified. Each doping element plays a different role in modifying the material properties from different aspects. More specifically, Mg and Al atoms have been successfully doped into the  $\text{LiCoO}_2$  lattice, altering the phase transition behaviour in the (de)lithiation process. Mg doping can also increase the electronic conductivity of the material. In contrast, even trace amounts of Ti cannot be completely incorporated into the  $\text{LiCoO}_2$  lattice. The segregation of Ti at the grain boundaries and on the surface, on the one hand, modifies the microstructure of the sample particle that is favourable for overall lithium diffusion and uniform internal strain distribution, and on the other hand, inhibits the oxygen activity and stabilizes the surface at high charging voltages. All of these effects synergistically add up to the remarkably improved electrochemical performances.

It can be inferred from this work that the rational design of electrode materials relies on comprehensive modifications from various aspects. Multiscale and multifaceted characterizations are the key to gaining insights into the roles of the modification elements, as well as the fundamental principles of the modification approaches. Moreover, as verified in this specific case, the low solubility of Ti and, thus, the segregation at the particle surface and grain boundaries, plays a vital role in electrochemical performance enhancement. The specific behaviour of Ti, which is beyond the conventional doping scenario, implies the necessity to revisit elements with a non-optimum solubility as dopants for material design and optimization. This would have profound implications for the design of electrode materials, well beyond the present case of high-voltage  $\text{LiCoO}_2$  cathodes for LIBs. Finally, it should be pointed out that, from the

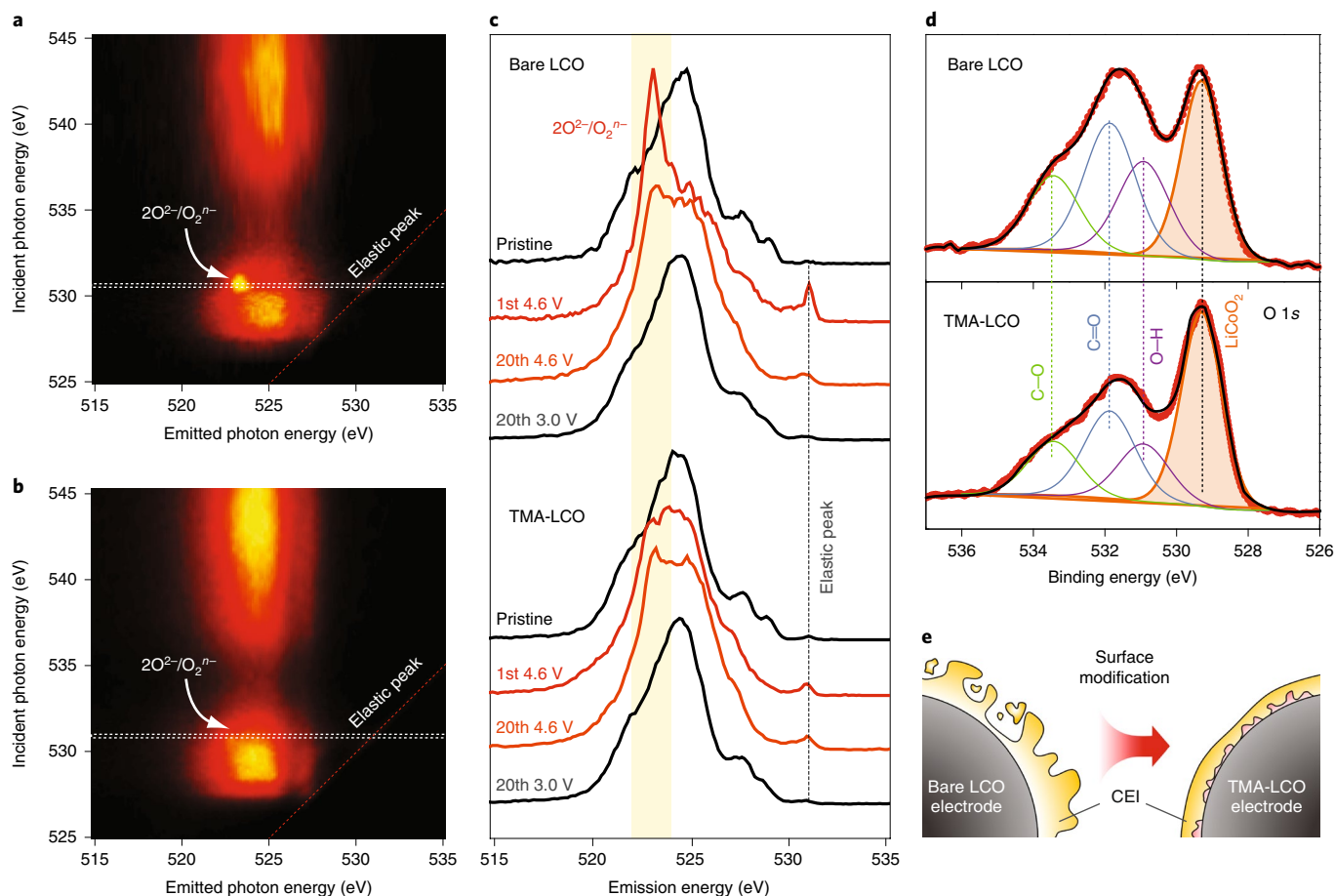


**Fig. 5 | Revealing the surface chemistry with soft X-ray spectroscopy.** **a, b**, O K edge RIXS maps collected on 4.6 V charged bare LCO (**a**) and TMA-LCO (**b**). With a low X-ray irradiation energy of  $\sim 529$  eV, O 1s electrons are excited into unoccupied Co 3d–O 2p hybridization states, whereas irradiation with high-energy X-rays ( $\sim 540$  eV) excites O 1s electrons into Co 4sp–O 2p hybridization states. The horizontal dashed lines indicate the excitation energy at which the RIXS spectra in **c** were collected (around 531 eV). **c**, RIXS spectra collected on bare LCO (top) and TMA-LCO (bottom) in pristine, 4.6 V charged states, and the 3.0 V discharged state after the 20th cycle with an X-ray excitation energy of 531 eV. The electrodes were prepared from cells cycled at a current rate of 0.1 C. **d**, O 1s XPS spectra of bare LCO (top) and TMA-LCO (bottom) electrodes after the 10th cycle at the 3.0 V discharged state. **e**, Schematic of the differences in CEI between bare LCO and TMA-LCO.

perspective of practical applications, the performances of LiCoO<sub>2</sub> at 4.6 V are still far from satisfactory. The development of high-energy-density LIBs with high-voltage LiCoO<sub>2</sub> requires comprehensive consideration of the cathode, anode, electrolyte and other key components, which calls for more research efforts and engineering considerations. Nonetheless, this work unfolds the promising future of dragging LiCoO<sub>2</sub> to even higher voltage and approaching the theoretical capacity limit for practical applications.

## Methods

**Material synthesis.** The LiCoO<sub>2</sub> materials were prepared by a solid-state reaction method using Li<sub>2</sub>CO<sub>3</sub> (99%), Co<sub>3</sub>O<sub>4</sub> (99.7%), Al<sub>2</sub>O<sub>3</sub> (99.9%), MgO (99%) and TiO<sub>2</sub> (99.9%) as precursors. All of the raw materials are industrial materials of battery grade. An excess of 5 wt% Li<sub>2</sub>CO<sub>3</sub> was used to compensate for the lithium loss during high-temperature synthesis. The starting materials were ground in an Agate mortar and the mixed powders were sintered at 1,000 °C for 10 h in an Alumina crucible to form the intermediate products. Then, the intermediate products were ground again in an Agate mortar and sintered for a second time at 900 °C for 10 h to obtain the final products.

**XRD and SEM characterization.** The XRD measurements were conducted using a Bruker D8 ADVANCE diffractometer with Cu K $\alpha$  radiation ( $\lambda = 1.5405$  Å) in the scan range ( $2\theta$ ) of 10–80°. For the in situ XRD experiments, a specially designed Swagelok cell equipped with an X-ray-transparent aluminium window was used for the in situ measurements. The in situ XRD patterns were collected with an interval of 40 min for each  $2\theta$  scan from 10–60° on charging and discharging at a current

rate of 0.1 C (1 C = 274 mA g<sup>-1</sup>). The morphologies of the samples were investigated by SEM (Hitachi S-4800).

**XPS characterization.** The XPS measurements were recorded with a spectrometer with Mg/Al K $\alpha$  radiation (ESCALAB 250 Xi; Thermo Fisher Scientific). All binding energies were calibrated using the C 1s peak of the Super P at 284.4 eV as an internal standard. To prevent air exposure, all samples were transferred using a transfer box provided by Thermo Fisher Scientific.

**TEM characterization.** The TEM/scanning TEM images, EDS and EELS measurements were performed using a JEOL ARM200F microscope operating at 200 kV, which was equipped with a probe-forming aberration corrector and Gatan image filter (GIF Quantum 965).

**Half-cell assembly.** The LiCoO<sub>2</sub>/Li half-cell tests were conducted using coin cells (CR2032), assembled in an argon-filled glove box. The working electrodes were prepared by coating the slurry mixture of active material (80 wt%), Super P (10 wt%) and polyvinylidene fluoride (10 wt%) on an aluminium current collector, followed by drying at 120 °C in a vacuum for 10 h. The loading of active material was controlled to between 3.0 and 4.0 mg cm<sup>-2</sup>. The electrolyte was a solution of 1 M LiPF<sub>6</sub> in ethylene and dimethyl carbonate (1:1 in volume). Lithium foil was used as the counter electrode, and Al<sub>2</sub>O<sub>3</sub>-coated polyethylene film was used as the separator.

**Full-cell assembly.** The LiCoO<sub>2</sub>/graphite full-cell tests were conducted using stacked pouch cells assembled in a dry room. The cathode electrodes were prepared by coating the mixture slurry of active material (95 wt%), carbon black

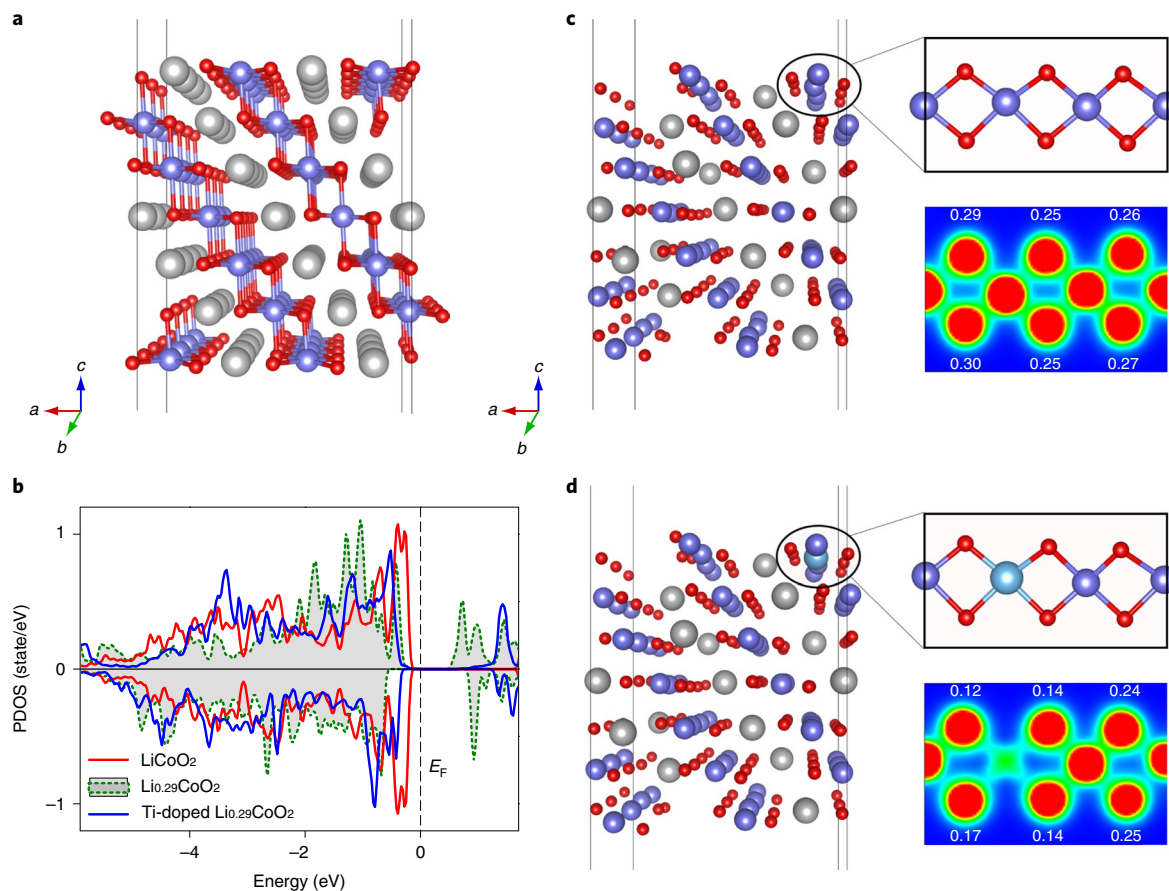


**Fig. 6 | Density functional theory calculations for Ti substitution that can modify the surface electronic structure.** **a**, Optimized atomic structure of the (104) slab of LiCoO<sub>2</sub>. The grey, blue and red spheres represent Li, Co and O atoms, respectively. **b**, Projected density of states (PDOS) values of the surface O atom at the (104) surface of LiCoO<sub>2</sub>, Li<sub>0.29</sub>CoO<sub>2</sub> and Ti-doped Li<sub>0.29</sub>CoO<sub>2</sub>. E<sub>F</sub> represents the Fermi level. **c,d**, Optimized atomic structures of the (104) slab of Li<sub>0.29</sub>CoO<sub>2</sub> (**c**) and Ti-doped (104) slab of Li<sub>0.29</sub>CoO<sub>2</sub> (**d**). The larger cyan sphere in **d** represents the Ti ion substituting the corresponding Co ion. The insets on the right-hand side for **c** and **d** are the top views of the corresponding surface structures (top) and surface charge density contours (bottom), respectively. The numbers on the charge density contours are the charge loss (in electrons) of the corresponding O atom on delithiation from LiCoO<sub>2</sub> to Li<sub>0.29</sub>CoO<sub>2</sub>, as obtained from Bader charge analysis.

(3 wt%) and polyvinylidene fluoride (2 wt%) on an aluminium current collector, followed by drying at 120 °C in a vacuum for 10 h. The areal capacity was controlled to between 3.5 and 3.8 mAh cm<sup>-2</sup>. The anode electrodes were composed of graphite (94.5 wt%), carbon black (2 wt%), carboxy methyl cellulose sodium (1.5 wt%) and styrene butadiene rubber (2 wt%), and fabricated following the same coating and drying procedures. The capacity ratio between negative electrode and positive electrode was controlled to between 1.05 and 1.08. The electrolyte and separator were the same as those used in the half cells.

**Electrochemical measurements.** The charge and discharge tests were carried out using a Land CT2001A battery test system in a voltage range of 3.0–4.6 V at various C rates at room temperature for the half cells. For the full-cell tests, a constant current and constant voltage mode was used. The cells were charged at 0.33 C to 4.55 V and then held until the current dropped to 0.1 C. The discharge process was conducted at a constant current mode at 0.33 C. The full cells were cycled at the first two cycles for the formation process. For the first cycle, the pouch cells were charged at 0.02 C for 2 h. After resting for 5 min, the cells were charged at 0.2 C to 4.55 V and then held at this voltage until the current dropped to 0.02 C (constant voltage process). Then, the cells were discharged at 0.2 C to 3 V and rested for 5 min. For the second cycle, the cells were charged at 0.2 C to 3.85 V and rested at 45 °C for 48 h to complete the formation process.

**Synchrotron 2D and 3D fluorescence measurements and data analysis.** Nano- and microfluorescence mapping were performed, respectively, at the Hard X-ray Nanoprobe Beamline of the National Synchrotron Light Source II at Brookhaven National Laboratory and Beamline 2-3 of the Stanford Synchrotron Radiation Lightsource at the SLAC National Accelerator Laboratory. The nanoprobe experiment was carried out at 9.6 keV by focusing the coherent monochromatic X-rays down to a 50-nm spot size using a Fresnel X-ray zone plate. Tomography

measurements were performed by collecting a total of 51 projections from –75° to 75°, with 3° intervals. The tomographic reconstruction was carried out using an iterative algorithm known as the algebraic reconstruction technique. Further visualization and quantification of the imaging data were carried out using the commercial software package Avizo. The segmentation of subdomains in the imaged particle was based on the concentration ratio between Co and Ti. As discussed in the main text, the regions rich in Ti form interconnected networks (Fig. 4c,f) that divide the particle into 50 subdomains (Fig. 4g). The microprobe experiment was carried out using a Kirkpatrick–Baez mirror focused X-ray spot of ~1 μm to image a large field of view covering many particles, to ensure statistical representativeness (Supplementary Fig. 11). The correlation analysis of Ti and Co distribution was coupled with principle component analysis to separate the Ti-rich domains from the area of nominal composition.

**Synchrotron soft X-ray spectroscopy.** Soft X-ray spectroscopy measurements were performed at Beamline 8.0.1 of the Advanced Light Source at the Lawrence Berkeley National Laboratory. The beamline is equipped with a spherical grating monochromator that supplies linearly polarized soft X-rays with a resolving power up to 6,000. The XAS spectra were collected in both TEY and TFY modes simultaneously. TEY is surface sensitive with a probing depth of ~10 nm, while TFY provides bulk information with a probing depth of ~150 nm. The energies of the O K edge XAS spectra were aligned based on O K edge of Fe<sub>2</sub>O<sub>3</sub> references. The spectra intensities were normalized to the beam flux measured by a gold mesh upstream. The RIXS experiments were carried out with the high-resolution RIXS system at Beamline 8.0.1 of the Advanced Light Source. The newly built-up system is equipped with a refocusing mirror, a spherical pre-mirror, a variable line-spacing grating and a high-resolution X-ray photon detector with entrance slitless design. The slitless operation improves the acceptance angle of the spectrograph and increases the throughput without compromising energy resolution. The incident

excitation energy scale was calibrated according to XAS of the Fe<sub>2</sub>O<sub>3</sub> reference sample, while the subsequent emission energy was calibrated using the elastically scattering line. The final datasets were presented on a 2D map, where the emission intensity was colour coded as a function of the incident excitation (ordinate) energy and emission energy (abscissa).

**First principles calculations.** All density functional theory calculations were performed with the Vienna ab initio Simulation Package<sup>36</sup>. The spin-polarized generalized gradient approximation (GGA) with PBE function<sup>37</sup> was used to treat the electron exchange–correlation interactions, and the projector-augmented wave approach<sup>38</sup> was used to take into account the electron–ion interactions. Since GGA cannot correctly reproduce the localized electronic states of the transition metal oxide materials, the GGA + *U* method was used<sup>39,40</sup>. The *U* values for the Co 3*d* and Ti 3*d* states were chosen to be 4.91 and 5.0 eV, respectively<sup>41,42</sup>. Furthermore, we included the Van der Waals interaction throughout the calculations. A plane-wave basis with a kinetic energy cut-off of 520 eV was used. The Monkhorst–Pack scheme<sup>43</sup>, with a 2 × 3 × 1 k-point mesh, was used for the integration in the irreducible Brillouin zone. The lattice parameters and ionic position were fully relaxed, and the final forces on all atoms were less than 0.01 eV Å<sup>-1</sup>. Density of states calculations were smeared using the Gaussian smearing method with a smearing width of 0.05 eV. The LiCoO<sub>2</sub> (104) surface was simulated using the symmetric periodic slab model containing 42 Li atoms, 84 O atoms and 42 Co atoms, with consecutive slabs separated by a 18 Å vacuum layer. The delithiated-state Li<sub>0.29</sub>CoO<sub>2</sub> was modelled by extracting 30 out of 42 Li ions from the LiCoO<sub>2</sub> slab system. The Ti-doped LiCoO<sub>2</sub>/Li<sub>0.29</sub>CoO<sub>2</sub> slab system was modelled by substituting 1 out of 42 Co ions with a Ti ion.

## Data availability

The data that support the plots within this paper and other finding of this study are available from the corresponding author upon reasonable request.

Received: 25 October 2018; Accepted: 9 May 2019;

Published online: 17 June 2019

## References

- Whittingham, M. S. Ultimate limits to intercalation reactions for lithium batteries. *Chem. Rev.* **114**, 11414–11443 (2014).
- Goodenough, J. B. Evolution of strategies for modern rechargeable batteries. *Acc. Chem. Res.* **46**, 1053–1061 (2013).
- Nitta, N., Wu, F., Lee, J. T. & Yushin, G. Li-ion battery materials: present and future. *Mater. Today* **18**, 252–264 (2015).
- Lin, F. et al. Metal segregation in hierarchically structured cathode materials for high-energy lithium batteries. *Nat. Energy* **1**, 15004 (2016).
- Lin, F. et al. Surface reconstruction and chemical evolution of stoichiometric layered cathode materials for lithium-ion batteries. *Nat. Commun.* **5**, 3529 (2014).
- Liu, C. F., Neale, Z. G. & Cao, G. Z. Understanding electrochemical potentials of cathode materials in rechargeable batteries. *Mater. Today* **19**, 109–123 (2016).
- Wang, D. W. et al. Synthetic control of kinetic reaction pathway and cationic ordering in high-Ni layered oxide cathodes. *Adv. Mater.* **29**, 1606715 (2017).
- Radin, M. D. et al. Narrowing the gap between theoretical and practical capacities in Li-ion layered oxide cathode materials. *Adv. Energy Mater.* **7**, 1602888 (2017).
- Kalluri, S. et al. Surface engineering strategies of layered LiCoO<sub>2</sub> cathode material to realize high-energy and high-voltage Li-ion cells. *Adv. Energy Mater.* **7**, 1601507 (2017).
- Gu, R. et al. Improved electrochemical performances of LiCoO<sub>2</sub> at elevated voltage and temperature with an in situ formed spinel coating layer. *ACS Appl. Mater. Interfaces* **10**, 31271–31279 (2018).
- Yano, A., Shikano, M., Ueda, A., Sakaebe, H. & Ogumi, Z. LiCoO<sub>2</sub> degradation behavior in the high-voltage phase transition region and improved reversibility with surface coating. *J. Electrochem. Soc.* **164**, A6116–A6122 (2017).
- Xu, Y. H. et al. In situ visualization of state-of-charge heterogeneity within a LiCoO<sub>2</sub> particle that evolves upon cycling at different rates. *ACS Energy Lett.* **2**, 1240–1245 (2017).
- MacNeil, D. D. & Dahn, J. R. The reactions of Li<sub>0.5</sub>CoO<sub>2</sub> with nonaqueous solvents at elevated temperatures. *J. Electrochem. Soc.* **149**, A912–A919 (2002).
- Doh, C.-H. et al. Thermal and electrochemical behaviour of C/Li<sub>x</sub>CoO<sub>2</sub> cell during safety test. *J. Power Sources* **175**, 881–885 (2008).
- Whittingham, M. S. Lithium batteries and cathode materials. *Chem. Rev.* **104**, 4271–4301 (2004).
- Liu, Q. et al. Approaching the capacity limit of lithium cobalt oxide in lithium ion batteries via lanthanum and aluminium doping. *Nat. Energy* **3**, 936–943 (2018).
- Lu, Y.-C., Mansour, A. N., Yabuuchi, N. & Shao-Horn, Y. Probing the origin of enhanced stability of “AlPO<sub>4</sub>” nanoparticle coated LiCoO<sub>2</sub> during cycling to high voltages: combined XRD and XPS studies. *Chem. Mater.* **21**, 4408–4424 (2009).
- Kalluri, S. et al. Feasibility of cathode surface coating technology for high-energy lithium-ion and beyond-lithium-ion batteries. *Adv. Mater.* **29**, 1605807 (2017).
- Wu, N., Zhang, Y., Wei, Y., Liu, H. & Wu, H. Template-engaged synthesis of 1D hierarchical chainlike LiCoO<sub>2</sub> cathode materials with enhanced high-voltage lithium storage capabilities. *ACS Appl. Mater. Interfaces* **8**, 25361–25368 (2016).
- Wang, F. et al. Stabilizing high voltage LiCoO<sub>2</sub> cathode in aqueous electrolyte with interphase-forming additive. *Energy Environ. Sci.* **9**, 3666–3673 (2016).
- Wang, J., Ji, Y. J., Appathurai, N., Zhou, J. G. & Yang, Y. Nanoscale chemical imaging of the additive effects on the interfaces of high-voltage LiCoO<sub>2</sub> composite electrodes. *Chem. Commun.* **53**, 8581–8584 (2017).
- Wang, L. L., Chen, B. B., Ma, J., Cui, G. L. & Chen, L. Q. Reviving lithium cobalt oxide-based lithium secondary batteries—toward a higher energy density. *Chem. Soc. Rev.* **47**, 6505–6602 (2018).
- Koyama, Y., Arai, H., Tanaka, I., Uchimoto, Y. & Ogumi, Z. First principles study of dopant solubility and defect chemistry in LiCoO<sub>2</sub>. *J. Mater. Chem. A* **2**, 11235–11245 (2014).
- Gopukumar, S., Jeong, Y. & Kim, K. B. Synthesis and electrochemical performance of tetravalent doped LiCoO<sub>2</sub> in lithium rechargeable cells. *Solid State Ion.* **159**, 223–232 (2003).
- Tukamoto, H. & West, A. R. Electronic conductivity of LiCoO<sub>2</sub> and its enhancement by magnesium doping. *J. Electrochem. Soc.* **144**, 3164–3168 (1997).
- Zou, M., Yoshio, M., Gopukumar, S. & Yamaki, J. Synthesis of high-voltage (4.5V) cycling doped LiCoO<sub>2</sub> for use in lithium rechargeable cells. *Chem. Mater.* **15**, 4699–4702 (2003).
- Kim, S. et al. Self-assembly of core-shell structures driven by low doping limit of Ti in LiCoO<sub>2</sub>: first-principles thermodynamic and experimental investigation. *Phys. Chem. Chem. Phys.* **19**, 4104–4113 (2017).
- Van der Ven, A., Aydinol, M. K., Ceder, G., Kresse, G. & Hafner, J. First-principles investigation of phase stability in Li<sub>x</sub>CoO<sub>2</sub>. *Phys. Rev. B* **58**, 2975–2987 (1998).
- Amatucci, G. G., Tarascon, J. M. & Klein, L. C. CoO<sub>2</sub>, the end member of the Li<sub>x</sub>CoO<sub>2</sub> solid solution. *J. Electrochem. Soc.* **143**, 1114–1123 (1996).
- Reimers, J. N. & Dahn, J. R. Electrochemical and in situ X-ray diffraction studies of lithium intercalation in Li<sub>x</sub>CoO<sub>2</sub>. *J. Electrochem. Soc.* **139**, 2091–2097 (1992).
- Yang, S.-H., Levasseur, S., Weill, F. & Delmas, C. Probing lithium and vacancy ordering in O3 layered Li<sub>x</sub>CoO<sub>2</sub> (x ≈ 0.5): an electron diffraction study. *J. Electrochem. Soc.* **150**, A366–A373 (2003).
- Yang, W. et al. Key electronic states in lithium battery materials probed by soft X-ray spectroscopy. *J. Electron Spectrosc.* **190**, 64–74 (2013).
- Yoon, W.-S. et al. Oxygen contribution on Li-ion intercalation–deintercalation in LiCoO<sub>2</sub> investigated by O K-edge and Co L-edge X-ray absorption spectroscopy. *J. Phys. Chem. B* **106**, 2526–2532 (2002).
- Kotani, A. & Shin, S. Resonant inelastic X-ray scattering spectra for electrons in solids. *Rev. Mod. Phys.* **73**, 203–246 (2001).
- Yang, W. & Devereaux, T. P. Anionic and cationic redox and interfaces in batteries: advances from soft X-ray absorption spectroscopy to resonant inelastic scattering. *J. Power Sources* **389**, 188–197 (2018).
- Kresse, G. & Furthmüller, J. Efficient iterative schemes for ab initio total-energy calculations using a plane-wave basis set. *Phys. Rev. B* **54**, 11169–11186 (1996).
- Perdew, J. P., Burke, K. & Ernzerhof, M. Generalized gradient approximation made simple. *Phys. Rev. Lett.* **77**, 3865–3868 (1996).
- Kresse, G. & Joubert, D. From ultrasoft pseudopotentials to the projector augmented-wave method. *Phys. Rev. B* **59**, 1758–1775 (1999).
- Anisimov, V. I., Zaanen, J. & Andersen, O. K. Band theory and Mott insulators: Hubbard U instead of Stoner I. *Phys. Rev. B* **44**, 943–954 (1991).
- Vladimir, I. A., Aryasetiawan, F. & Lichtenstein, A. I. First-principles calculations of the electronic structure and spectra of strongly correlated systems: the LDA + *U* method. *J. Phys. Condens. Matter* **9**, 767–808 (1997).
- Zhou, F., Cococcioni, M., Marianetti, C. A., Morgan, D. & Ceder, G. First-principles prediction of redox potentials in transition-metal compounds with LDA + *U*. *Phys. Rev. B* **70**, 235121 (2004).
- Tanaka, S. et al. Atomic and electronic structures of Li<sub>1-x</sub>Ti<sub>0.12</sub>/Li<sub>1-x</sub>Ti<sub>0.12</sub> (001) interfaces by first-principles calculations. *J. Mater. Sci.* **49**, 4032–4037 (2014).
- Monkhorst, H. J. & Pack, J. D. Special points for Brillouin-zone integrations. *Phys. Rev. B* **13**, 5188–5192 (1976).

## Acknowledgements

This work was supported by funding from the National Key R&D Program of China (grant number 2016YFB0100100), National Natural Science Foundation of China (grant numbers 51822211, 11564016 and 11574281) and Foundation for Innovative Research Groups of the National Natural Science Foundation of China (grant number 51421002). The work done at BNL was supported by the Assistant Secretary for Energy Efficiency

and Renewable Energy, Vehicle Technology Office of the US Department of Energy through the BMR Program, including the Battery500 Consortium under contract DE-SC0012704. Use of the National Synchrotron Light Source II is supported by the US Department of Energy, an Office of Science user Facility operated by Brookhaven National Laboratory under contract number DE-SC0012704. The SLAC National Accelerator Laboratory is supported by the US Department of Energy, Office of Science, Office of Basic Energy Sciences under contract number DE-AC02-76SF00515. Use of the Stanford Synchrotron Radiation Lightsource, SLAC National Accelerator Laboratory, is supported by the US Department of Energy, Office of Science, Office of Basic Energy Sciences under contract number DE-AC02-76SF00515. Soft X-ray spectroscopic data were collected at beamline 8.0.1 of the Advanced Light Source, which is supported by the Director, Office of Science, Office of Basic Energy Sciences of the US Department of Energy under contract number DE-AC02-05CH11231. We gratefully acknowledge help from beamlines BL14W1 and BL08U at Shanghai Synchrotron Radiation Facility.

### Author's contributions

X.Y. and H.L. conceived the idea; J.-N.Z. synthesized the materials and performed electrochemistry measurements and X-ray diffraction measurements; C.M. performed the TEM measurements and analysis; Y.L., M.G., Xiaojing.H., S.L. and Y.C. performed

the transmission X-ray microscopy measurement and data analysis; Q.L. and W.Y. performed the soft X-ray spectroscopy experiment and data analysis; C.O. and R.X. performed the density functional theory analysis; Q.L., X.Y., J.-N.Z., Y.L. and C.O. wrote the paper with critical inputs from all other authors. All authors edited and approved the manuscript.

### Competing interests

The authors declare no competing interests.

### Additional information

**Supplementary information** is available for this paper at <https://doi.org/10.1038/s41560-019-0409-z>.

**Reprints and permissions information** is available at [www.nature.com/reprints](http://www.nature.com/reprints).

**Correspondence and requests for materials** should be addressed to X.Y., Y.L. or H.L.

**Publisher's note:** Springer Nature remains neutral with regard to jurisdictional claims in published maps and institutional affiliations.

© The Author(s), under exclusive licence to Springer Nature Limited 2019